APPLIED PHYSICS

Stable organic thin-film transistors

Xiaojia Jia, Canek Fuentes-Hernandez, Cheng-Yin Wang, Youngrak Park, Bernard Kippelen*

Organic thin-film transistors (OTFTs) can be fabricated at moderate temperatures and through cost-effective solution-based processes on a wide range of low-cost flexible and deformable substrates. Although the charge mobility of state-of-the-art OTFTs is superior to that of amorphous silicon and approaches that of amorphous oxide thin-film transistors (TFTs), their operational stability generally remains inferior and a point of concern for their commercial deployment. We report on an exhaustive characterization of OTFTs with an ultrathin bilayer gate dielectric comprising the amorphous fluoropolymer CYTOP and an Al_2O_3:HfO_2 nanolaminate. Threshold voltage shifts measured at room temperature over time periods up to 5.9×10^5 s do not vary monotonically and remain below 0.2 V in microcrystalline OTFTs (μc-OTFTs) with field-effect carrier mobility values up to 1.6 cm^2 V^{-1} s^{-1}. Modeling of these shifts as a function of time with a double stretched-exponential (DSE) function suggests that two compensating aging mechanisms are at play and responsible for this high stability. The measured threshold voltage shifts at temperatures up to 75°C represent at least a one-order-of-magnitude improvement in the operational stability over previous reports, bringing OTFT technologies to a performance level comparable to that reported in the scientific literature for other commercial TFTs technologies.

INTRODUCTION

From smartphones to flat-panel TVs, thin-film transistors (TFTs) are a core technology of modern displays (1–3). TFTs are also becoming an enabling technology for radio frequency identification (4) and a wide range of sensing applications (5–7). The commercial adoption of TFT technologies was enabled by the use of hydrogenated amorphous silicon (a-Si:H) (2). However, a-Si:H TFTs exhibit limited carrier mobility (μ), with values in the range of 0.5 to 1 cm^2 V^{-1} s^{-1} (2), hindering the development of fast-switching circuits. They also suffer from large threshold voltage (V_{TH}) instabilities that can be mitigated by using circuit-based compensation schemes but at the expense of the simplicity of backplane circuit designs (8, 9). To overcome these limitations, research and development efforts in recent years have focused on TFTs based on other semiconductor materials such as microcrystalline Si (μc-Si) (10), polycrystalline Si (poly-Si) (11), amorphous oxides (a-oxides) (1), and organic semiconductors (12–15).

To date, poly-Si and a-oxide TFTs have found their way into commercial display products because of their large μ values and superior V_{TH} stability when compared to those displayed by a-Si:H TFTs. In contrast, although μ values of state-of-the-art microcrystalline (small molecule) or nearly amorphous (conjugated polymer) organic thin-film transistors (OTFTs) now surpass those found in a-Si:H TFTs and approach those found in some a-oxide TFTs (16–18), their V_{TH} stability remains inferior to that displayed by a-Si:H TFTs and constitutes an important point of concern toward their wide commercial deployment and adoption (12, 19).

The primary mechanism behind V_{TH} instability in OTFTs arises from the trapping of charge carriers or molecular species (such as oxygen or water) at defect sites located at microcrystalline boundaries, nanometer-sized voids (due to porosity), or at the semiconductor-dielectric interface (20, 21). To date, many approaches to reduce or passivate these trap sites include the use of postprocessing thermal annealing (22) and amorphous fluoropolymers (for example, CYTOP) as gate dielectric layers (23). Although the use of CYTOP leads to OTFTs with reduced bias stress effects (24), devices with a single CYTOP dielectric layer typically also operate at high voltages and display shifts of

V_{TH} that monotonically vary in time (20). Very recently, the use of molecular additives has been shown to lead to OTFTs with a greatly improved environmental stability and with an operational stability comparable to that displayed by single-crystal organic field-effect transistors (sc-organic FETs) (19). This is significant because, before this recent report, only in the absence of crystalline boundaries and porosity, such as in sc-organic FETs, have OTFTs been able to display V_{TH} stability superior to that of a-Si:H TFTs (14). Although previous studies have shown that μc-OTFTs can display stability comparable or superior to that of "low-temperature" (150° to 350°C) processed a-Si:H and metal-oxide TFTs under moderate-bias conditions (that is, $V_{GS} \gg V_{DS}$) (25), under high-bias conditions (that is, $V_{GS} = V_{DS}$), the degradation is generally more severe. Hence, under high-bias conditions, even sc-organic FETs and OTFTs using molecular additives have shown to date a V_{TH} stability that is inferior to that reported in the scientific literature for other commercial TFT technologies, in particular, μc-Si, a-oxide, and poly-Si TFTs (the last displaying the most stable performance of all TFT technologies) (26).

In the past, we introduced an approach that enabled low-voltage operation and improved environmental and operational stability of μc-OTFTs (15, 20). This approach consists of using a bilayer gate dielectric (for example, CYTOP/metal oxide) instead of the commonly used single-layer gate dielectric (for example, CYTOP or metal oxide) and has been proven effective in OTFTs with channel layers comprising either small molecules (20, 27), polymers (13), or small-molecule/polymer blends (13, 20). In the bilayer gate dielectric approach, the second dielectric layer appears to compensate for the shift of V_{TH} induced by the trapping of carriers, thereby introducing a second mechanism that produces an opposite V_{TH} shift over time (for example, charge accumulation within the dielectric layer by slowly oriented dipoles). Specifically, we have shown that, when this second gate dielectric layer comprises a single metal oxide (for example, Al_2O_3) processed by atomic layer deposition (ALD), n- and p-channel μc-OTFTs operate at low-voltage values with good operational stability and excellent environmental stability, remaining functional after being subjected to oxygen plasma for several minutes and being immersed in water for several hours (13). Furthermore, when the second gate dielectric layer comprises a first layer of Al_2O_3 by ALD, deposited on CYTOP, and a second nanolaminate (NL) layer comprising nanometer-thick alternating

Center for Organic Photonics and Electronics, School of Electrical and Computer Engineering, Georgia Institute of Technology, Atlanta, GA 30332, USA.
*Corresponding author. Email: kippelen@gatech.edu

layers of Al_2O_3 and HfO_2 by ALD, μc-OTFTs can even sustain immersion in water at 95°C for tens of minutes (12). Here, we build on this approach by showing that μc-OTFTs with an optimized bilayer gate dielectric comprised of a first CYTOP layer and a second Al_2O_3:HfO_2 NL layer grown by ALD display improved environmental stability and unprecedented operational stability, with V_{TH} shifts that are comparable to or smaller than the ones reported in the scientific literature for μc-Si and a-oxide TFTs over time. Furthermore, the small V_{TH} shifts displayed by these μc-OTFTs are weakly dependent on temperature variations at least up to 50°C above room temperature (RT), thus highlighting the robustness of this approach.

RESULTS

Figure 1A shows the architecture of top-gate bottom-contact μc-OTFTs. The detailed fabrication process is described in Materials and Methods. The devices in this work are named with the letters "A," "B," and "C" to indicate specific device geometries and followed by "_#" to indicate the NL layer thickness. In A_# and B_# devices, the semiconductor layer is composed of a 6,13-bis(triisopropylsilylethynyl)–pentacene (TIPS-pentance)/poly[bis(4-phenyl) (2,4,6-trimethylphenyl) amine] (PTAA) blend, and in C_# devices, the semiconductor layer is composed of a 2,8-difluoro-5,11-bis(triethylsilylethynyl) anthradithiophene (diF-TES-ADT)/PTAA blend. The gate dielectric layer in A_# and C_# devices is composed of CYTOP (35 nm)/ALD Al_2O_3:HfO_2 NL (# nm). The ALD NL layer was synthesized at 110°C by the repeated alternation of five ALD cycles of Al_2O_3 and five ALD cycles of HfO_2.

As a reference, we also fabricated TIPS-pentacene/PTAA μc-OTFTs having the gate dielectric geometry that we recently reported (12): CYTOP (35 nm)/ALD Al_2O_3 (20 nm)/ALD NL (44 nm), herein referred to as B_44 devices. The properties of type A and B μc-OTFTs with different NL thickness values are presented in the Supplementary Materials.

The pristine transfer characteristics of champion A_33 and C_33 μc-OTFTs measured in a N_2-filled glove box are shown in Fig. 1B. All devices exhibited hysteresis-free electrical characteristics. Figure 1C summarizes statistical values of the electrical parameters for pristine μc-OTFTs of all types (W/L = 2550 μm/180 μm). The electrical parameters of A_33 μc-OTFTs are comparable to those measured in B_44 μc-OTFTs (see fig. S1 and table S1) and to those measured in TIPS-pentacene/PTAA–based μc-OTFTs having a CYTOP/ALD-oxide bilayer gate dielectric (12, 20). C_33 devices also display similar performance parameters to previously reported diF-TES-ADT/PTAA–based μc-OTFTs with a CYTOP/ALD Al_2O_3 bilayer gate dielectric (13).

In the past, we had shown that μc-OTFTs with a CYTOP/Al_2O_3/NL gate dielectric (that is, B_44 μc-OTFTs) exhibited superior environmental stability (when immersed in near-boiling water) in comparison to those with a CYTOP/Al_2O_3 gate dielectric (12). Here, first, we conduct a direct comparison of the environmental stability of A_33, C_33, and B_44 μc-OTFTs before and after exposure to two different environmental conditions: (i) air with a relative humidity (RH) of 35% for 1 day and (ii) immersion in distilled water for 16 hours. Figure 1D shows the normalized temporal changes of the source-to-drain current, $I_{DS}(t)/I_{DS}(0) \equiv 1 + \Delta I_{DS}(t)$, measured on champion devices
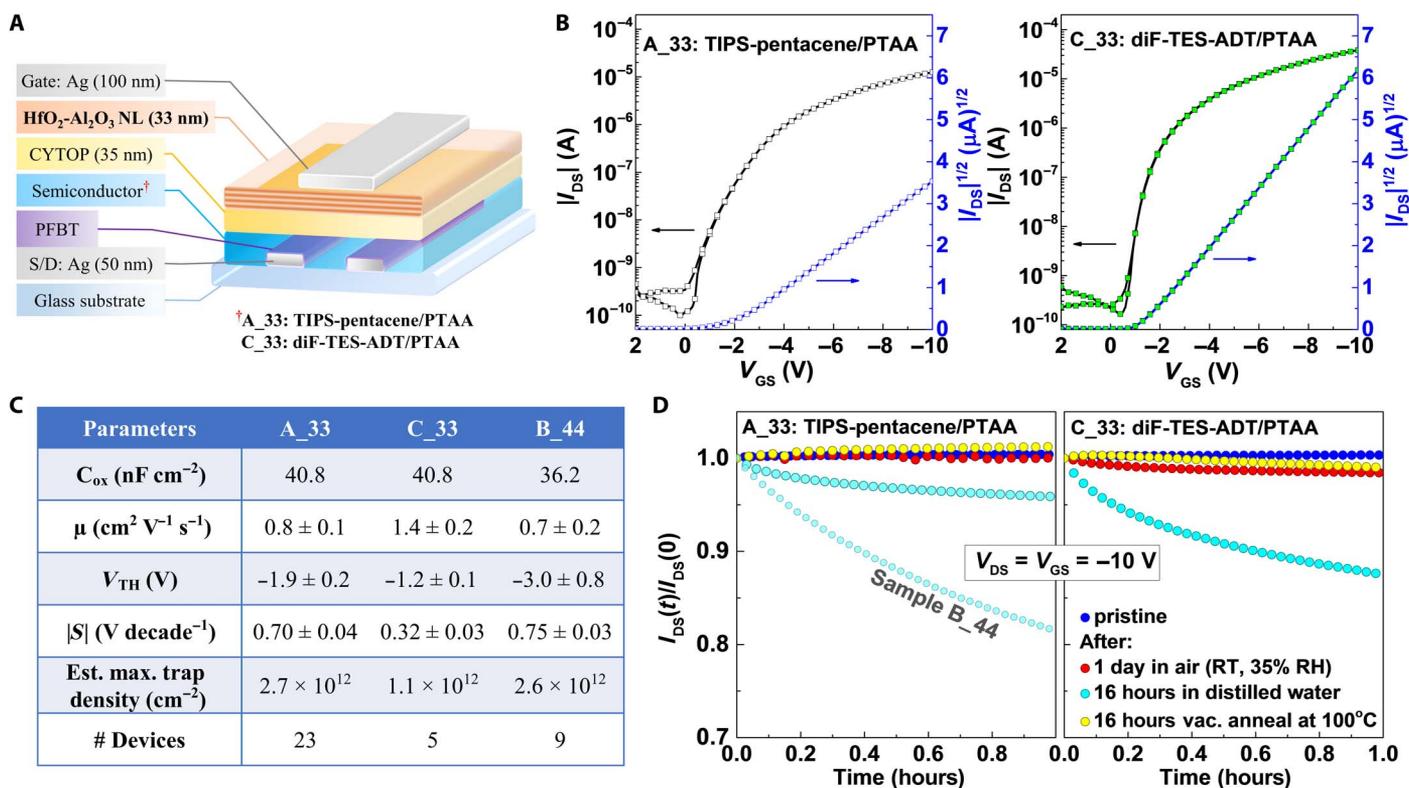
Fig. 1. General electrical properties and environmental stability. (A) The structure of top-gate bottom-contact μc-OTFTs with gate dielectric layers of CYTOP/NL. The semiconductor layers of A_33 and C_33 are TIPS-pentacene/PTAA blend and diF-TES-ADT/PTAA blend, respectively. (B) Transfer characteristics of as-fabricated μc-OTFTs of A_33 (left) and C_33 (right). (C) Electrical parameters of A_33, C_33, and B_44. (D) Environmental stability under continuous dc-bias stress for μc-OTFTs under different ambient conditions.

in the saturation regime (that is, on-state gate bias stress, $V_{DS} = V_{GS} = -10$ V) for 1 hour. Air exposure produces $|\Delta I_{DS}(t)| < 1\%$ on A_33, C_33, and B_44 (shown in fig. S3) μc-OTFTs. In contrast, prolonged immersion in water (16 hours) results in larger $|\Delta I_{DS}(1 \text{ hour})|$ values, with changes in B_44 devices found to be significantly larger (ca. 20 to 35%) than those observed in A_33 (ca. 4 to 8%) and C_33 (ca. 12%) devices. These changes were not permanent but were reversible after devices were vacuum-annealed at 100°C for 16 hours. These trends are qualitatively consistent with our previous reports where, for instance, μc-OTFTs having a CYTOP/ALD Al_2O_3 gate dielectric yielded $|\Delta I_{DS}$ (10 min)$| > 10\%$ after immersion in water for 16 hours (13), significantly larger than $|\Delta I_{DS}(1 \text{ hour})|$ values in A_33, C_33, and B_44 devices. Hence, whereas it is clear that water absorbed during prolonged exposure leads to degradation of the device operational stability under continuous bias stress, the presence of single ALD Al_2O_3 layers in the architecture of a μc-OTFT (for example, B_44 μc-OTFTs) also leads to increased device sensitivity due to the presence of water in the environment. Therefore, the device architecture of A_33 and C_33 devices is not only less complex than that of B_44 devices but also leads to superior environmental stability.

Next, we turn to the long-term operational stability of A_33 μc-OTFTs. Figure 2 (A and B) shows the temporal evolution of $I_{DS}(t)/I_{DS}(0)$ during continuous on-state gate bias stress test in the saturation regime ($V_{DS} = V_{GS} = -10$ V) for 40 hours and in the linear regime ($V_{DS} = -2$ V, $V_{GS} = -10$ V) for 100 hours. In both regimes, A_33 devices exhibit high stability, with $|\Delta I_{DS}(t)| < 4\%$ after tens of hours of continuous operation. Note that the operational stability is dependent on the bias conditions (that is, V_{GS} and V_{DS}) and channel sheet resistance, as reported by Bisoyi et al. (25). Here, under high-bias conditions ($V_{GS} = V_{DS}$) and

with a channel sheet resistance of 10 megaohms/square, measured I_{DS} changes are below 4% even after stress times in the 10^5-s range. Furthermore, operational stability tests shown in fig. S9, on devices with a smaller channel length of 85 μm, reveal I_{DS} changes below 1% after similar stress times in the 10^5-s range. Hence, in contrast to previous studies (25), our devices do not reach the 10% I_{DS} decay lifetime after comparable stress times.

To rationalize the temporal changes of $I_{DS}(t)$ and to extrapolate the long-term stability of these μc-OTFTs, first, it is necessary to validate a model that describes these changes. In contrast to μc-OTFTs with a single gate dielectric layer, we have suggested that μc-OTFTs with a bilayer gate dielectric are subject to two distinct mechanisms that can lead to a change of properties over time (20). The first one, more commonly reported, causes a decrease of $I_{DS}(t)/I_{DS}(0)$ during continuous dc-bias stress due to charge trapping at or around the semiconductor-dielectric interface (9, 14). This contribution is described by assuming that $V_{TH}(t)$ follows a single stretched-exponential (SSE) model (eq. S1). In our devices, we observe a second effect causing $I_{DS}(t)/I_{DS}(0)$ to increase over time (13). The latter effect is observed regardless of channel morphology (that is, small molecules, polymers, or small-molecule/polymer blends) and type of transport in the channel (that is, n- or p-channel) (12, 13) and even in OTFTs having CYTOP/HfO_2 bilayer gate dielectrics (see fig. S5). Although the specific physical mechanism remains unclear at this point, the effect appears general. Furthermore, as we show below, it can be controlled by varying the metal oxide layer thickness and modeled by assuming that $V_{TH}(t)$ also follows an SSE functional form (eq. S2) but with opposite sign to the one attributed to the first effect (eq. S1) as the second effect compensates for the effect of trapping. In view of these considerations, we define the following
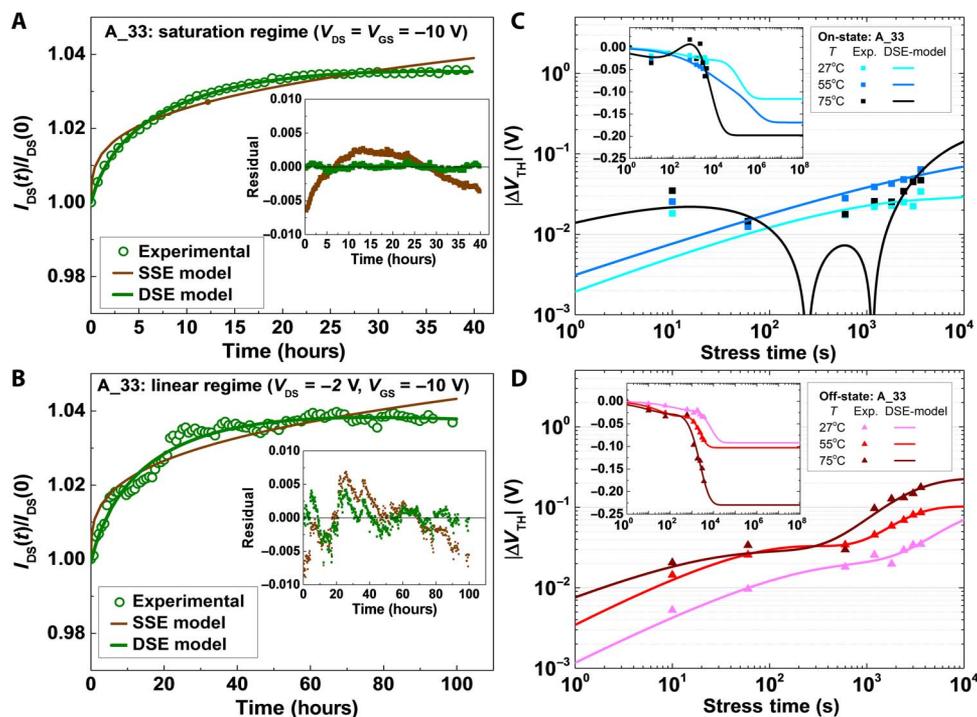

Fig. 2. Operational and temperature stability in N_2 during continuous dc-bias stress. Temporal evolution of the normalized I_{DS} during dc-bias stress (**A**) at saturation regime ($V_{DS} = V_{GS} = -10$ V) for 40 hours with fitted curves and (**B**) at linear regime ($V_{DS} = -2$ V, $V_{GS} = -10$ V) for 100 hours with fitted curves. The insets show the fitting residuals of the SSE model (brown) and the DSE model (green). The $|\Delta V_{TH}|$ values after dc-bias stress of as-fabricated A_33 devices (**C**) at on-state ($V_{DS} = V_{GS} = -10$ V) and (**D**) at off-state ($V_{DS} = 0$ V, $V_{GS} = 10$ V) bias stress tests under different temperatures in the dark, with curves fitted from corresponding ΔV_{TH} values using the DSE model (see insets).

analytical expression for $\Delta V_{TH}(t)$, which we refer to as the double stretched-exponential (DSE) model

$$\Delta V_{TH}(t) = \Delta V_{TH,1\infty} \cdot \left\{ 1 - \exp\left[-\left(\frac{t}{\tau_1}\right)^{\beta_1} \right] \right\}$$
$$+ \Delta V_{TH,2\infty} \cdot \left\{ 1 - \exp\left[-\left(\frac{t}{\tau_2}\right)^{\beta_2} \right] \right\} \quad (1)$$

where τ_i are the characteristic decay times, β_i are the dispersion parameters ($0 < \beta_i < 1$), and $\Delta V_{TH,i\infty} = [V_{TH,i}(\infty) - V_{TH}(0)]$ is the threshold voltage change expected as time tends to infinity ($i = 1$ or 2). Equations S4 and S5 present $V_{TH}(t)$-related analytical expressions for $I_{DS}(t)$ in the linear and saturation regimes, respectively (9, 28, 29). Figure 2 (A and B) displays a comparison of the best fits to the experimental data and the residuals (insets) using the SSE and DSE models. This comparison reveals that the DSE model better describes $I_{DS}(t)$ under on-state dc-bias stress than the SSE model, particularly in the saturation regime and at a longer time. Figure S6 confirms these observations for a wider range of OTFT geometries. The parameters used to fit the data using both models are presented in tables S2 and S3. We note that, as shown in figs. S4 and S5, the operational stability of I_{DS} depends on the gate dielectric geometry, that is, the thickness of the NL, and consequently can be tailored. Because of practical constraints, values of $\Delta V_{TH,i\infty}$ cannot be unequivocally determined using this fitting procedure. Instead, the ratio $m = \Delta V_{TH,1\infty}/\Delta V_{TH,2\infty}$ can be derived. We have found this ratio to be dependent on the NL layer's thickness, with devices displaying improved stability when $m \approx 1$. However, values of τ_i and β_i are less dependent on the NL thickness and are remarkably similar for both contributions to $\Delta V_{TH}(t)$, with τ_i values in the range of 10^4 s and β_i values in the range of ca. 0.4 to 0.6. Figure S8 shows the contributions of the two opposite aging mechanisms, $\Delta V_{TH,1}(t)$ and $\Delta V_{TH,2}(t)$, of devices with different gate dielectric geometries under on-state bias stress. This similarity in the dynamics of both competing processes is unique if compared to other previous systems reported in the literature (28) and allows the thickness of the NL to be used as a parameter to optimize the long-term stability of these OTFTs.

Next, we focus our attention on V_{TH} changes occurring during positive and negative bias temperature stress tests, critical for assessing the operational stability of a TFT technology (8). Here, to avoid confusion between biasing conditions for n- or p-type TFTs, we refer to these tests as on- and off-state temperature stress tests. Figure 2 (C and D) shows ΔV_{TH} and $|\Delta V_{TH}|$ measured in the dark on as-fabricated A_33 devices during on-state ($V_{DS} = V_{GS} = -10$ V) and off-state ($V_{DS} = 0$ V, $V_{GS} = 10$ V) bias-temperature stress tests for 1 hour, respectively. Figure S10 shows the transfer characteristics measured during these tests, which reveal that an increase in temperature more prominently results in increased off-current values that can be attributed to an increased gate dielectric leakage current, as shown in fig. S11. However, smaller changes of V_{TH} can also be observed even after the temperature is increased by ca. 50°C, and $|\Delta V_{TH}(1 \text{ hour})|$ is less than 0.07 V during on-state temperature stress tests and smaller than 0.2 V during off-state temperature stress tests. Measured $\Delta V_{TH}(t)$ values during on- and off-state temperature stress tests were also fitted using the DSE model and extrapolated to a stress time of over 10 years, as shown in the insets of Fig. 2 (C and D). Table S5 displays values of parameters used in these fits. At 27°C, the values of parameters τ_i and

m are slightly smaller than those found on previous I_{DS} bias stress effect studies. We attribute these differences to the different experimental procedures used to measure temporal I_{DS} changes and that used to derive $\Delta V_{TH}(t)$ in bias stress tests, in one case by modeling I_{DS} changes during continuous bias stress and in the other one by suspending the bias stress to measure changes in the transfer characteristics by sweeping the gate voltage from the positive to negative and then back to positive voltages. To illustrate the second process, fig. S12 shows the temporal I_{DS} changes, including the interruptions to measure the transfer characteristics. This method produces predominantly negative $V_{TH}(t)$ shifts after measurement of the transfer characteristics and leads to I_{DS} characteristics over time that are qualitatively different from those measured during constant bias stress. Furthermore, it should be pointed out that these small $\Delta V_{TH}(t)$ values are also related to a device's bias-stress history, as shown in fig. S13 for another batch of A_33 devices and for C_33 devices. With this in mind, although it is clear that at this point further systematic studies would be necessary to derive the physical insights that allow rationalizing the thermal dependence of $|\Delta V_{TH}|$, it is also clear that regardless of bias condition or device history, $|\Delta V_{TH}|$ in all devices tested remains less than 0.15 V during on-state stress tests for 1 hour. Hence, the $|\Delta V_{TH}|$ values during on-state stress tests measured in A_33 and C_33 μc-OTFTs are around the same order of magnitude with the ones displayed by state-of-the-art a-oxide TFTs (for example, $|\Delta V_{TH}| > 0.01$ V during on-state stress tests at 70°C for 1 hour) (30).

Finally, we carried out independent long-term on-bias stress tests ($V_{DS} = V_{GS} = -10$ V) at RT (ca. 27°C) on pristine A_33 and C_33 μc-OTFTs. The transfer characteristics measured during these tests are shown in fig. S7 and reveal only very small changes. Table S2 provides a comparison of the electrical parameters (that is, μ, V_{TH}, $|S|$, and current on/off ratio) derived from these transfer characteristics before and after stress tests. After stress, the values of μ, V_{TH}, and $|S|$ are changed by less than 3%. Figure 3A shows measured ΔV_{TH} values as well as the DSE-modeled values extrapolated to a stress time of over 10 years. The values of the fitting parameters are shown in table S6. In addition, Fig. 3A shows the DSE-modeled ΔV_{TH} values derived from fits to the experimental data in Fig. 2A. These results demonstrate that good consistency is obtained within one order of magnitude between the ΔV_{TH} values measured on different batches of devices, with different organic semiconductor layers and using slightly different experimental methods. The left panel of Fig. 3B shows the experimental $|\Delta V_{TH}|$ values of A_33 and C_33 μc-OTFTs in a log-log scale with fitted curves from Fig. 3A and, for comparison, extrapolated SSE-modeled $|\Delta V_{TH}|$ derived for organic single-crystal N,N'-bis(n-alkyl)-(1,7 and 1,6)-dicyanoperylene-3,4:9,10-bis(dicarboximide)s (PDIF-CN$_2$) (sc-PDIF-CN$_2$) TFTs (14) and the state-of-the-art OTFTs using indacenodithiophene-co-benzothiadiazole (IDTBT) with tetrafluoro-tetracyanoquinodimethane (F4TCNQ) molecular additives (19). Even considering device-to-device variations, $|\Delta V_{TH}|$ values measured in all μc-OTFTs are at least an order of magnitude smaller than those expected from sc-organic FETs or the state-of-the-art OTFTs with molecular additives. Furthermore, the right panel of Fig. 3B shows a comparison of the DSE-modeled $|\Delta V_{TH}|$ values derived from fits to the experimental data at 55°C displayed in Fig. 2C for our μc-OTFTs, with SSE-modeled $|\Delta V_{TH}|$ values for other commercial TFT technologies at 50°C [$I_{DS} \geq 10$ μA; for self-consistency, taken from the study of Arai and Sasaoka (26)]. We recognize that direct benchmarking of our results to conventional inorganic TFT technologies is challenged by the lack of detailed stability reports on widely used commercial products in the scientific literature. Hence, comparison can only be made to previously published results generated in an academic
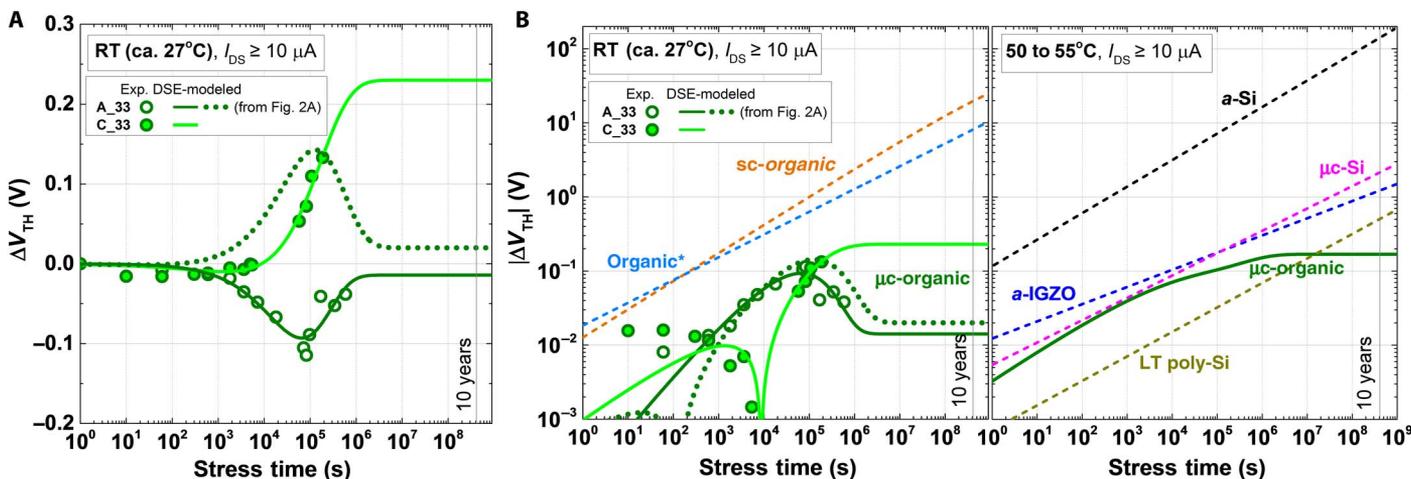
Fig. 3. Long-term stability comparison in different TFT technologies. (**A**) RT measured ΔV_{TH} under on-state bias stress tests of A_33 and C_33 at $V_{DS} = V_{GS} = -10$ V with fitted curves using a DSE model. (**B**) Left: RT measured $|\Delta V_{TH}|$ under on-state bias stress tests of A_33 and C_33 at $V_{DS} = V_{GS} = -10$ V with fitted curves from (A). "*" represents the blue dashed data that are from the state-of-the-art OTFT showing the highest stability by using IDTBT with F4TCNQ molecular additives (19). The orange dashed data are from the sc-organic FET with remarkable stability (14). Right: Comparison between DSE-modeled $|\Delta V_{TH}|$ at 55°C for μc-OTFTs and SSE-modeled $|\Delta V_{TH}|$ at 50°C for commercial TFT technologies (26).

environment, but it may not necessarily constitute a fair direct comparison to the state-of-the-art today for mature commercial technologies.

DISCUSSION

In summary, we have demonstrated an effective approach to realize solution-processed top-gate μc-OTFTs that have an engineered bilayer gate dielectric comprising a CYTOP layer and an NL fabricated by ALD. These μc-OTFTs, processed at temperatures below 110°C, display improved environmental stability (particular under aqueous environments) when compared to previously reported μc-OTFTs and an unprecedented level of operational (V_{TH}) stability, superior to values reported in the scientific literature for a-Si TFTs and comparable to other commercial TFT technologies. Although it is clear that further studies will be necessary to improve our understanding of the physical mechanisms giving rise to the temporal and thermal dependence of the ΔV_{TH} observed, we have shown here that the metal oxide layer thickness can be effectively used to tailor these effects and that the temporal dynamics of ΔV_{TH} can be modeled by two competing processes that appear to display similar dynamics and magnitude in bilayers of CYTOP and Al_2O_3:HfO_2 NL. These results suggest that μc-OTFTs can achieve the level of performance of commercial inorganic semiconductor-based TFT technologies. In addition, we believe that using a similar approach could further benefit the operational stability of such TFT technologies. Note that the stability studies reported here were carried out with prolonged continuous bias conditions. In many applications such as backplane technology for displays, the devices operate most of the time in a pulsed mode with bias voltages with alternating polarity. Bias conditions are likely to further influence the overall stability, and therefore, it would be useful to conduct further studies for a given application with specific conditions.

MATERIALS AND METHODS
Device fabrication
All the μc-OTFT devices with CYTOP/ALD-oxide bilayer dielectrics were fabricated on glass substrates (Corning Eagle XG),

which were cleaned by sonication in acetone, deionized water, and isopropanol for 5 min for each step beforehand. Fifty-nanometer-thick source and drain electrodes of Ag were deposited on the substrates through shadow masks, using a Kurt J. Lesker SPECTROS thermal evaporator at a deposition rate of 1 Å s^{-1} under 5×10^{-7} torr at RT. To form a self-assembled monolayer of pentafluorobenzenthiol (PFBT) on Ag electrodes, we immersed the substrates with sources and drain electrodes into a 10 mM PFBT solution in ethanol for 15 min and then rinsed them in pure ethanol for 1 min followed by annealing at 60°C on a hot plate for 5 min in a N_2-filled glove box in devices with a channel length of 180 μm. In the devices with a shorter channel length (85 μm), the electrodes were coated with a 10-nm-thick evaporated MoO_x layer to further increase charge injection and reduce contact resistance. To prepare the solution for the organic semiconductor layer, we dissolved a 1:1 weight ratio of PTAA (Sigma-Aldrich) and TIPS-pentacene (Sigma-Aldrich) or diF-TES-ADT (Lumtec) blend in 1,2,3,4-tetrahydronaphthalene (anhydrous, 99%) (Tetralin; Sigma-Aldrich) for a concentration of 30 mg ml^{-1}. A 70-nm-thick active semiconducting layer was deposited by spin-coating TIPS-pentacene/PTAA or diF-TES-ADT/PTAA solution (filtered with a 0.2-μm filter) at 500 rpm for 10 s with 500 rpm s^{-1} acceleration and 2000 rpm for 20 s with 1000 rpm s^{-1} acceleration, followed by annealing at 100°C on a hot plate for 15 min in a N_2-filled glove box. The as-purchased 9 weight % (wt %) CYTOP (Asahi Glass, CTL-890M) was diluted with the solvent CT-SOLV180 (Asahi Glass) in a 1:3.5 volume ratio to have a 2 wt % CYTOP, which was spin-coated on top of the semiconductor layer at 3000 rpm for 60 s with 10000 rpm s^{-1} acceleration, followed by annealing at 100°C for 10 min on a hot plate in a N_2-filled glove box. The final thickness of CYTOP film was 35 nm. For samples A_33, C_33, A_27, and A_22, after CYTOP deposition, an Al_2O_3-HfO_2 NL was deposited in a Savannah 100 ALD system from Cambridge NanoTech by alternating five cycles of Al_2O_3 and five cycles of HfO_2 for 30 times (A_33 and C_33), 25 times (A_27), and 20 times (A_22) at 110°C, producing films of 33, 27.5, and 22 nm, respectively. For samples B_44, B_22, and B_11, a 20-nm-thick Al_2O_3 film was deposited as a nucleation layer, followed by depositing an Al_2O_3-HfO_2 NL at 110°C. The NL films were deposited by alternating five

cycles of Al_2O_3 and five cycles of HfO_2 for 40 times (B_44), 20 times (B_22), and 10 times (B_11), producing films of 44, 22, and 22 nm, respectively. Finally, 100-nm-thick gate electrodes of Ag were deposited on the substrates through a shadow mask, using a Kurt J. Lesker SPECTROS thermal evaporator at a deposition rate of 1 Å s^{-1} at a base pressure of $<5 \times 10^{-7}$ torr at RT.

Electrical characterization

All the μc-OTFT devices were characterized using an Agilent E5272A source/monitor unit at RT inside a N_2-filled glove box, in which both O_2 and H_2O values were maintained below 0.1 parts per million to avoid ambient humidity and oxygen. The capacitance densities of gate dielectrics were extracted by measuring and linear-fitting the capacitance values of the capacitors having six different areas using a precision inductance-capacitance-resistance (LCR) meter (Agilent 4284A). The dielectric constant values were 2.0 for CYTOP and 8.9 for Al_2O_3, which were previously reported (20, 31, 32). The extracted dielectric constant value of Al_2O_3-HfO_2 NL was around 10.5. The capacitance density of the gate dielectric for each sample shown in table S1 was close to the theoretical value estimated from series-connected capacitors of stacked dielectric layers.

Environmental reliability characterization

To investigate the environmental reliability of μc-OTFT devices, A_33, C_33, and B_44 were exposed to different conditions as follows: air with an RH of 35% for 1 day, immersion in distilled water for 16 hours, and vacuum annealing at 100°C for 16 hours. At each interval, each sample was briefly transferred back into a N_2-filled glove box, and the dc-bias stress reliability was tested immediately.

SUPPLEMENTARY MATERIALS

Supplementary material for this article is available at http://advances.sciencemag.org/cgi/content/full/4/1/eaao1705/DC1

REFERENCES AND NOTES

1. A. Nathan, S. Lee, S. Jeon, J. Robertson, Amorphous oxide semiconductor TFTs for displays and imaging. *J. Disp. Technol.* **10**, 917–927 (2014).

2. A. Nathan, A. Kumar, K. Sakariya, P. Servati, S. Sambandan, D. Striakhilev, Amorphous silicon thin film transistor circuit integration for organic LED displays on glass and plastic. *IEEE J. Solid-State Circuits* **39**, 1477–1486 (2004).

3. C. D. Sheraw, L. Zhou, J. R. Huang, D. J. Gundlach, T. N. Jackson, Organic thin-film transistor-driven polymer-dispersed liquid crystal displays on flexible polymeric substrates. *Appl. Phys. Lett.* **80**, 1088–1090 (2002).

4. K. Myny, S. Steudel, S. Smout, P. Vicca, F. Furthner, B. van der Putten, A. K. Tripathi, G. H. Gelinck, J. Genoe, W. Dehaene, P. Heremans, Organic RFID transponder chip with data rate compatible with electronic product coding. *Org. Electron.* **11**, 1176–1179 (2010).

5. M. Yun, A. Sharma, C. Fuentes-Hernandez, D. K. Hwang, A. Dindar, S. Singh, S. Choi, B. Kippelen, Stable organic field-effect transistors for continuous and nondestructive sensing of chemical and biologically relevant molecules in aqueous environment. *ACS Appl. Mater. Interfaces* **6**, 1616–1622 (2014).

6. T. Someya, T. Sekitani, S. Iba, Y. Kato, H. Kawaguchi, T. Sakurai, A large-area, flexible pressure sensor matrix with organic field-effect transistors for artificial skin applications. *Proc. Natl. Acad. Sci. U.S.A.* **101**, 9966–9970 (2004).

7. M. E. Roberts, S. C. B. Mannsfeld, N. Queraltó, C. Reese, J. Locklin, W. Knoll, Z. Bao, Water-stable organic transistors and their application in chemical and biological sensors. *Proc. Natl. Acad. Sci. U.S.A.* **105**, 12134–12139 (2008).

8. S. C. Deane, R. B. Wehrspohn, M. J. Powell, Unification of the time and temperature dependence of dangling-bond-defect creation and removal in amorphous-silicon thin-film transistors. *Phys. Rev. B* **58**, 12625–12628 (1998).

9. F. R. Libsch, J. Kanicki, Bias-stress-induced stretched-exponential time dependence of charge injection and trapping in amorphous thin-film transistors. *Appl. Phys. Lett.* **62**, 1286–1288 (1993).

10. B. G. Choi, K.-T. Kim, J. H. Bae, S. Lee, H. K. Lee, S. K. Kim, K.-S. Park, C.-D. Kim, Y. K. Hwang, I.-J. Chung, High performance micro-crystalline silicon TFT using indirect thermal crystallization technique. *ECS Trans.* **33**, 213–216 (2010).

11. S. Xu, Z. Sun, D. Zhang, M. Wang, Reliability of low-temperature polysilicon thin-film transistors for flexible electronics application, in *2016 IEEE International Nanoelectronics Conference (INEC'16)* (IEEE, 2016), pp. 1–2.

12. C.-Y. Wang, C. Fuentes-Hernandez, M. Yun, A. Singh, A. Dindar, S. Choi, S. Graham, B. Kippelen, Organic field-effect transistors with a bilayer gate dielectric comprising an oxide nanolaminate grown by atomic layer deposition. *ACS Appl. Mater. Interfaces* **8**, 29872–29876 (2016).

13. D. K. Hwang, C. Fuentes-Hernandez, M. Fenoll, M. Yun, J. Park, J. W. Shim, K. A. Knauer, A. Dindar, H. Kim, Y. Kim, J. Kim, H. Cheun, M. M. Payne, S. Graham, S. Im, J. E. Anthony, B. Kippelen, Systematic reliability study of top-gate p- and n-channel organic field-effect transistors. *ACS Appl. Mater. Interfaces* **6**, 3378–3386 (2014).

14. M. Barra, F. V. Di Girolamo, N. A. Minder, I. Gutiérrez Lezama, Z. Chen, A. Facchetti, A. F. Morpurgo, A. Cassinese, Very low bias stress in *n*-type organic single-crystal transistors. *Appl. Phys. Lett.* **100**, 133301 (2012).

15. C.-Y. Wang, C. Fuentes-Hernandez, W.-F. Chou, B. Kippelen, Top-gate organic field-effect transistors fabricated on paper with high operational stability. *Org. Electron.* **41**, 340–344 (2017).

16. Y. Li, P. Sonar, L. Murphy, W. Hong, High mobility diketopyrrolopyrrole (DPP)-based organic semiconductor materials for organic thin film transistors and photovoltaics. *Energ. Environ. Sci.* **6**, 1684–1710 (2013).

17. H.-R. Tseng, H. Phan, C. Luo, M. Wang, L. A. Perez, S. N. Patel, L. Ying, E. J. Kramer, T.-Q. Nguyen, G. C. Bazan, A. J. Heeger, High-mobility field-effect transistors fabricated with macroscopic aligned semiconducting polymers. *Adv. Mater.* **26**, 2993–2998 (2014).

18. Z. Yi, S. Wang, Y. Liu, Design of high-mobility diketopyrrolopyrrole-based π-conjugated copolymers for organic thin-film transistors. *Adv. Mater.* **27**, 3589–3606 (2015).

19. M. Nikolka, I. Nasrallah, B. Rose, M. K. Ravva, K. Broch, A. Sadhanala, D. Harkin, J. Charmet, M. Hurhangee, A. Brown, S. Illig, P. Too, J. Jongman, I. McCulloch, J.-L. Bredas, H. Sirringhaus, High operational and environmental stability of high-mobility conjugated polymer field-effect transistors through the use of molecular additives. *Nat. Mater.* **16**, 356–362 (2017).

20. D. K. Hwang, C. Fuentes-Hernandez, J. Kim, W. J. Potscavage Jr., S.-J. Kim, B. Kippelen, Top-gate organic field-effect transistors with high environmental and operational stability. *Adv. Mater.* **23**, 1293–1298 (2011).

21. B. Lee, A. Wan, D. Mastrogiovanni, J. E. Anthony, E. Garfunkel, V. Podzorov, Origin of the bias stress instability in single-crystal organic field-effect transistors. *Phys. Rev. B* **82**, 085302 (2010).

22. J.-H. Bae, J. Park, C.-M. Keum, W.-H. Kim, M.-H. Kim, S.-O. Kim, S. K. Kwon, S.-D. Lee, Thermal annealing effect on the crack development and the stability of 6,13-bis(triisopropylsilylethynyl)-pentacene field-effect transistors with a solution-processed polymer insulator. *Org. Electron.* **11**, 784–788 (2010).

23. C.-Y. Wang, C. Fuentes-Hernandez, J.-C. Liu, A. Dindar, S. Choi, J. P. Youngblood, R. J. Moon, B. Kippelen, Stable low-voltage operation top-gate organic field-effect transistors on cellulose nanocrystal substrates. *ACS Appl. Mater. Interfaces* **7**, 4804–4808 (2015).

24. W. L. Kalb, T. Mathis, S. Haas, A. F. Stassen, B. Batlogg, Organic small molecule field-effect transistors with Cytop™ gate dielectric: Eliminating gate bias stress effects. *Appl. Phys. Lett.* **90**, 092104 (2007).

25. S. Bisoyi, U. Zschieschang, M. J. Kang, K. Takimiya, H. Klauk, S. P. Tiwari, Bias-stress stability of low-voltage p-channel and n-channel organic thin-film transistors on flexible plastic substrates. *Org. Electron.* **15**, 3173–3182 (2014).

26. T. Arai, T. Sasaoka, 49.1: Invited paper: Emergent oxide TFT technologies for next-generation AM-OLED displays. *SID Symp. Dig. Tech. Pap.* **42**, 710–713 (2011).

27. D. K. Hwang, R. R. Dasari, M. Fenoll, V. Alain-Rizzo, A. Dindar, J. W. Shim, N. Deb, C. Fuentes-Hernandez, S. Barlow, D. G. Bucknall, P. Audebert, S. R. Marder, B. Kippelen, Stable solution-processed molecular *n*-channel organic field-effect transistors. *Adv. Mater.* **24**, 4445–4450 (2012).

28. K. Fukuda, T. Suzuki, T. Kobayashi, D. Kumaki, S. Tokito, Suppression of threshold voltage shifts in organic thin-film transistors with bilayer gate dielectrics. *Phys. Stat. Sol. (A)* **210**, 839–844 (2013).

29. S. G. J. Mathijssen, M. Cölle, H. Gomes, E. C. P. Smits, B. de Boer, I. McCulloch, P. A. Bobbert, D. M. de Leeuw, Dynamics of threshold voltage shifts in organic and amorphous silicon field-effect transistors. *Adv. Mater.* **19**, 2785–2789 (2007).

30. E. K.-H. Yu, K. Abe, H. Kumomi, J. Kanicki, AC bias-temperature stability of a-InGaZnO thin-film transistors with metal source/drain recessed electrodes. *IEEE Trans. Electron Devices* **61**, 806–812 (2014).

31. X.-H. Zhang, W. J. Potscavage Jr., S. Choi, B. Kippelen, Low-voltage flexible organic complementary inverters with high noise margin and high dc gain. *Appl. Phys. Lett.* **94**, 043312 (2009).

32. R. Hamilton, J. Smith, S. Ogier, M. Heeney, J. E. Anthony, I. McCulloch, J. Veres, D. D. C. Bradley, T. D. Anthopoulos, High-performance polymer-small molecule blend organic transistors. *Adv. Mater.* **21**, 1166–1171 (2009).

33. M. McDowell, I. G. Hill, J. E. McDermott, S. L. Bernasek, J. Schwartz, Improved organic thin-film transistor performance using novel self-assembled monolayers. *Appl. Phys. Lett.* **88**, 073505 (2006).

34. G. Williams, D. C. Watts, S. B. Dev, A. M. North, Further considerations of non symmetrical dielectric relaxation behaviour arising from a simple empirical decay function. *Trans. Faraday Soc.* **67**, 1323–1335 (1971).

Citation: X. Jia, C. Fuentes-Hernandez, C.-Y. Wang, Y. Park, B. Kippelen, Stable organic thin-film transistors. *Sci. Adv.* **4**, eaao1705 (2018).

Science Advances

Stable organic thin-film transistors

Xiaojia Jia, Canek Fuentes-Hernandez, Cheng-Yin Wang, Youngrak Park and Bernard Kippelen

ARTICLE TOOLS	http://advances.sciencemag.org/content/4/1/eaao1705
SUPPLEMENTARY MATERIALS	http://advances.sciencemag.org/content/suppl/2018/01/08/4.1.eaao1705.DC1
REFERENCES	This article cites 33 articles, 3 of which you can access for free http://advances.sciencemag.org/content/4/1/eaao1705#BIBL
PERMISSIONS	http://www.sciencemag.org/help/reprints-and-permissions

Use of this article is subject to the Terms of Service